ACS APPLIED MATERIALS & INTERFACES

www.acsami.org

Forum Article

Dual-Modal Fe_xCu_ySe and Upconversion Nanoparticle Assemblies for Intracellular MicroRNA-21 Detection

Xiaoqian Jiang, Changlong Hao, Hongyu Zhang, Xiaoling Wu,* Liguang Xu, Maozhong Sun, Chuanlai Xu, and Hua Kuang*

Cite This: https://dx.doi.org/10.1021/acsami.0c00434

Read Online

ACCESS | Metrics & More | Article Recommendations | Supporting Information

ABSTRACT: In situ quantification and imaging of low-level intracellular microRNAs (miRs) are important areas in biosensor research. Herein, DNA-driven Fe_xCu_ySe@upconversion nanoparticle (UCNP) core@satellite nanostructures were developed to probe microRNA-21 (miR-21). Fe_xCu_ySe@UCNP probes displayed dual signals: upconversion luminescence (UCL) and magnetic resonance imaging (MRI). In the presence of miR-21, the luminescence signal was restored and the T_2 value was significantly increased because of dissociation of UCNPs from the assemblies. There was a good linear relationship between the dual signals and the expression levels of miR-21 in the range of 0.035−31.824 amol/ng_{RNA}. The limit of detection (LOD) was 0.0058 amol/ng_{RNA} for the luminescence intensity and 0.0182 amol/ng_{RNA} for the MRI signal. This method opens a new avenue for intracellular miR-21 detection with high sensitivity and specificity.

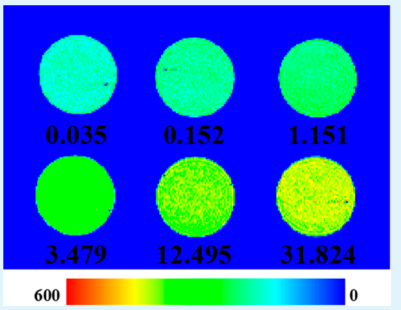

KEYWORDS: *Fe_xCu_ySe, upconversion nanoparticles, assemblies, intracellular, nicroRNA-21, detection*

INTRODUCTION

MicroRNAs (miRs) are short, single-stranded, endogenous, noncoding RNAs that serve as important biomarkers for cancer diagnosis.[1−3] Therefore, visualization and quantification of miRs benefits biochemical studies and clinical diagnosis. However, their low abundance, facile degradation and similar sequences make intracellular miRs difficult to detect.[4] Traditional methods for detection mainly include microarray crossover and quantitative real-time PCR (qRT-PCR), but these procedures are cumbersome, expensive, limited in terms of sensitivity, and have high operational requirements, which limit their application.[5,6]

Therefore, a method with high sensitivity and specificity for in situ quantification and imaging of miRs in living cells is urgently needed. In recent years, an increasing number of nanoprobes of various signal types have been used for miR detection, including Raman probes and fluorescence probes.[7−9] Fluorescent probes have received much attention because of their nondestructive testing, ease of operation, and in situ quantification.[10] Although probes based on organic fluorescent dyes have been used for in situ quantification and imaging, they have some drawbacks including instability, short lifetime, and background interference.[11,12] Upconversion nanoparticles (UCNPs) are novel imaging probes with benefits including near-infrared excitation, high photostability, low toxicity, and low background interference.[13−15] Through DNA hybridization, various nanostructures have been fabricated using UCNPs as building blocks. For example, Au-UCNP heterodimers, Au-UCNP pyramids, and AuNR@UCNP core@satellite structures have been developed to quantify various biomarkers in living cells.[16−19] However, most reported probes only offer single-signal detection.[20−22]

Multimodal imaging could overcome the shortcomings of single-mode imaging, provide more accurate information and improve the efficiency of disease diagnosis.[23−25] Besides optical imaging, magnetic resonance imaging (MRI) is a powerful method for noninvasive diagnosis, attracting great interest.[26−29] Iron nanoparticles (NPs) usually measure contrast ability based on T_2 value and T_2-weighted images.[30−33] Additionally, UCNPs containing the element Gd have been used to prepare T_1-weighted contrast agents.[34−37] The size, composition, morphology, and aggregation state of magnetite NPs can be controlled to improve the sensitivity for MRI.[38−41] For example, Cu_xFe_ySe-polyethylene glycol (PEG) was injected into mice harboring breast cancer (4T1) for MRI imaging,[42] and self-assembled $NaGdF_4$−$CaCO_3$ nanoconjugates offer outstanding contrast for tumor visualization through MRI, with on/off switching capabilities.[43] A core−shell structure consisting of $NaYF_4$ (Yb^{3+} and Tm^{3+}) and Fe_xO_y was previously designed for MRI and upconversion luminescence (UCL), and successfully applied to the lymphatic system.[44]

Special Issue: Translational DNA Nanotechnology

Received: January 13, 2020
Accepted: March 16, 2020

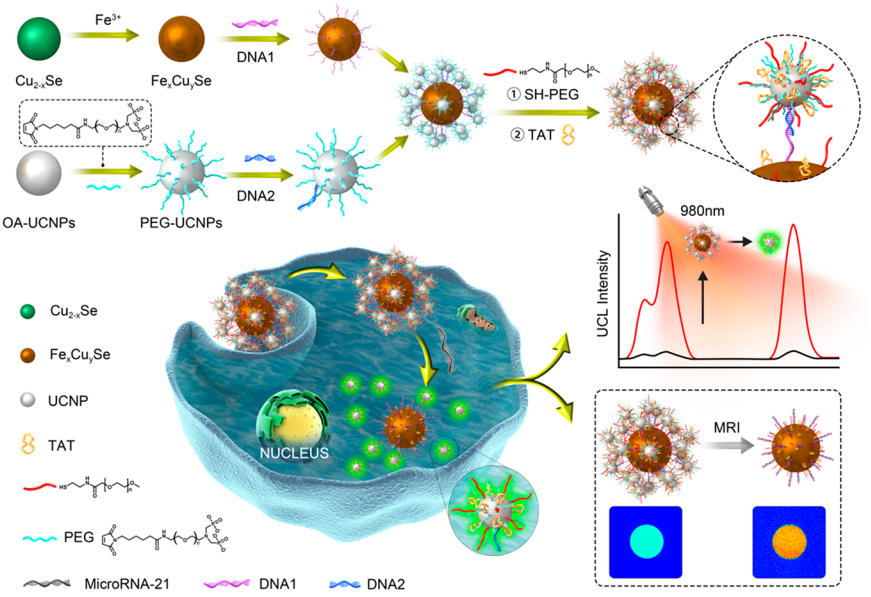

Figure 1. Schematic illustration of Fe_xCu_ySe@UCNP core@satellite structures for intracellular miR-21 detection.

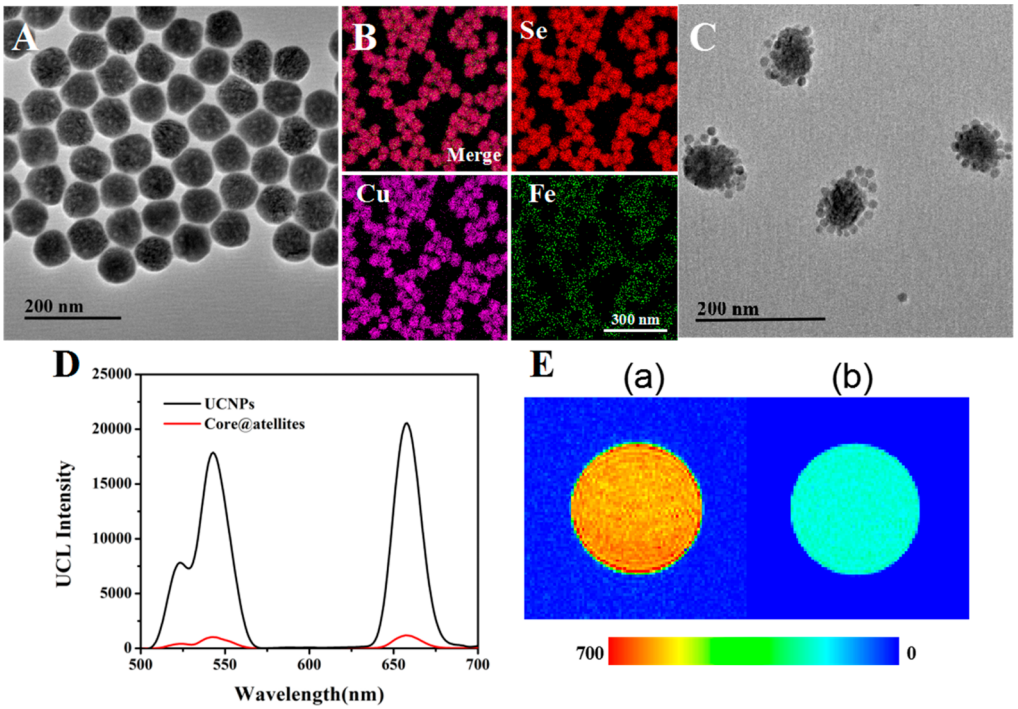

Figure 2. (A) TEM image and (B) EDX mapping of Fe_xCu_ySe in buffer. (C) TEM image of core@satellite structures assembled by Fe_xCu_ySe and UCNPs in buffer. (D) UCL spectra of core@satellite structures and UCNPs. (E) Color-processed T_2-weighted images of (a) Fe_xCu_ySe and (b) core@satellite structures.

Fe_xCu_ySe NPs are good contrast agents for MRI imaging, and they were employed herein as building blocks because of their excellent biosafety. In this context, DNA-driven Fe_xCu_ySe@UCNP nanoassemblies were fabricated that displayed dual UCL and MRI signals for the detection of microRNA-21 (miR-21) in living cells.

EXPERIMENTAL SECTION

Preparation of Fe_xCu_ySe Modified with DNA. In 10 mM TRIS-HCl buffer, DNA1 was added to Fe_xCu_ySe (DNA:Fe_xCu_ySe molar ratio = 500:1) and incubated at 37 °C for 12 h. The resulting Fe_xCu_ySe NPs were centrifuged several times and resuspended in buffer for subsequent use.

Preparation of UCNPs Modified with DNA. UCNPs were added to 10 mM TRIS-HCl buffer and DNA2 was added at a DNA2:UCNP molar ratio of 50:1 and incubated at 37 °C for 12 h. The mixture was centrifuged several times (9000 g, 10 min each time) and concentrated in buffer for subsequent use.

Preparation of Core@Satellite Structures. At a volume ratio of 1:1, purified Fe_xCu_ySe modified with DNA1 and UCNPs modified with DNA2 were mixed in TRIS-HCl buffer and incubated at 37 °C for 8 h. The resulting Fe_xCu_ySe@UCNP core@satellite structures were centrifuged several times and resuspended in TRIS-HCl buffer for subsequent use.

https://dx.doi.org/10.1021/acsami.0c00434
ACS Appl. Mater. Interfaces XXXX, XXX, XXX−XXX

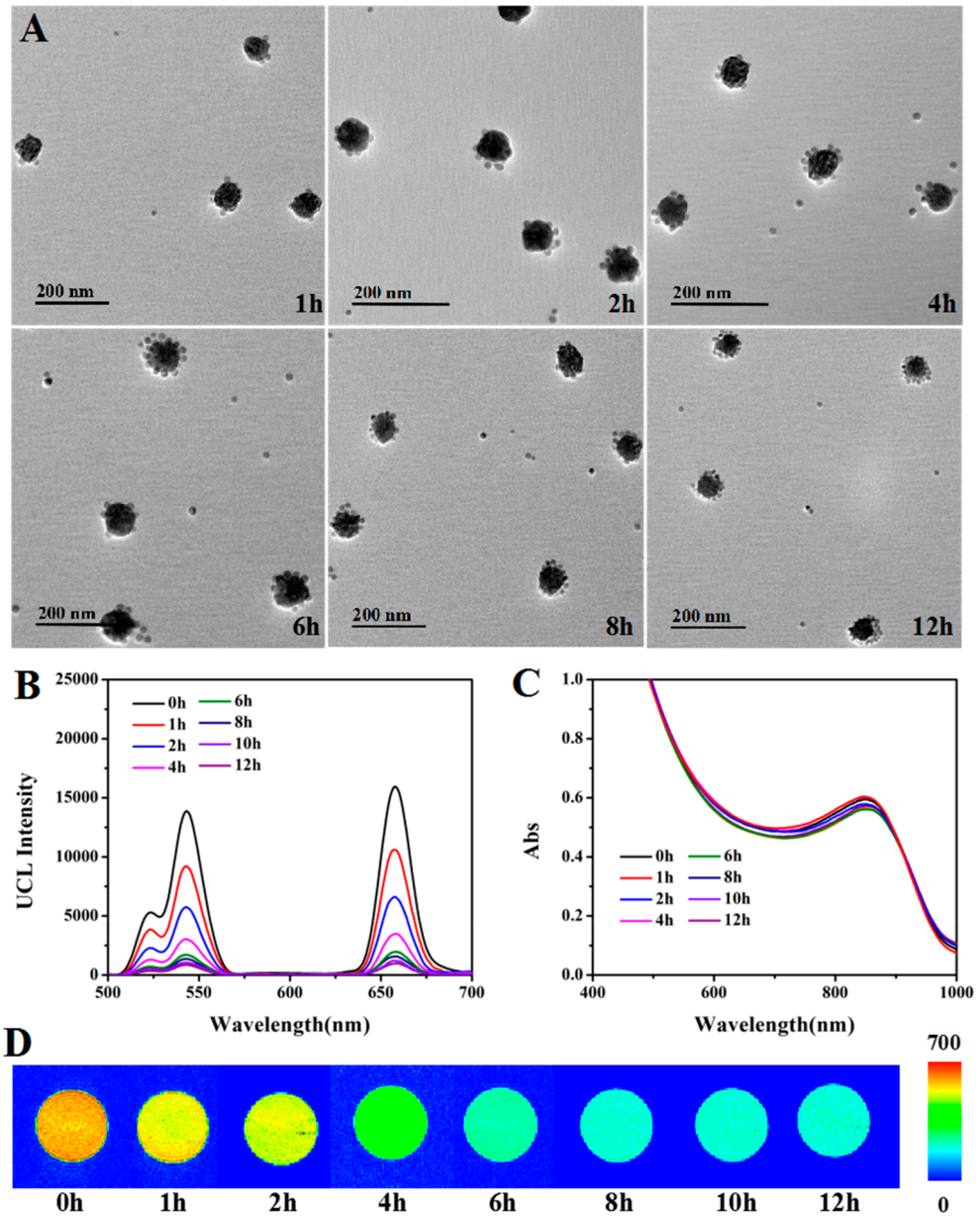

Figure 3. (A) TEM images, (B) UCL spectra, (C) UV−Vis absorption spectra, and (D) color-processed T_2-weighted images of the assembly process of core@satellite structures.

MicroRNA-21 Detection In Vitro. Core@satellite structures were added to nine 1.5 mL centrifuge tubes (500 μL each) and synthetic miR-21 (20 μM) was added and incubated at 37 °C for 2 h. The final concentrations of miR-21 were 0, 1, 2, 5, 10, 50, 100, 200, and 500 pM. The UCL intensity was measured using a fluorescence spectrometer with a 980 nm excitation laser. The measurement parameters for T_2-weighted images were repetition time = 1500 ms, echo time = 50 ms, and slice thickness = 6 mm. T_2 values were determined by inversion of the T_2 relaxation time curve.

MicroRNA-21 Detection in MCF-7 Cells. According to the procedure supplied with the LipofectamineRNAiMAX transfection reagent kit (Life Technologies), human breast cancer (MCF-7) cells were transfected with different amounts of miR-21 or antisense miR-21. After culturing for 24 h, total RNA was extracted and reverse-transcribed. The final content of miR-21 in MCF-7 cells was determined by qRT-PCR. Next, MCF-7 cells with different amounts of miR-21 were seeded into laser confocal dishes and incubated at 37 °C for 12 h. Core@satellite nanoprobes (1.5 mg/mL) were added to dishes and incubated at 37 °C for 8 h. The UCL intensity of cells was measured by confocal microscopy with a 980 nm excitation laser. In addition, MCF-7 cells with different amounts of miR-21 were seeded into 6-well plates and cultured for 12 h, and core@satellite nanoprobes (1.5 mg/mL) were added to plates and incubated at 37 °C for 8 h. Cells were collected in 1× Dulbecco's phosphate-buffered saline (DPBS, Life Technologies) to measure the UCL intensity using a fluorescence spectrophotometer. Meanwhile, cells were collected in 0.5% agarose for MRI scanning.

RESULTS AND DISCUSSION

Principles of Intracellular MicroRNA-21 Detection. Fe_xCu_ySe magnetic NPs were selected as the core for core@satellite structures. Fe_xCu_ySe NPs were synthesized by doping Fe^{3+} into $Cu_{2-x}Se$ NPs. Water-soluble UCNPs were acquired by modifying maleimide-PEG-phosphate ligand (Figure 1). The core@satellite structures were assembled using partially complementary DNA1 and DNA2 (Table S1) which were modified on the surface of Fe_xCu_ySe NPs and UCNPs,

https://dx.doi.org/10.1021/acsami.0c00434
ACS Appl. Mater. Interfaces XXXX, XXX, XXX−XXX

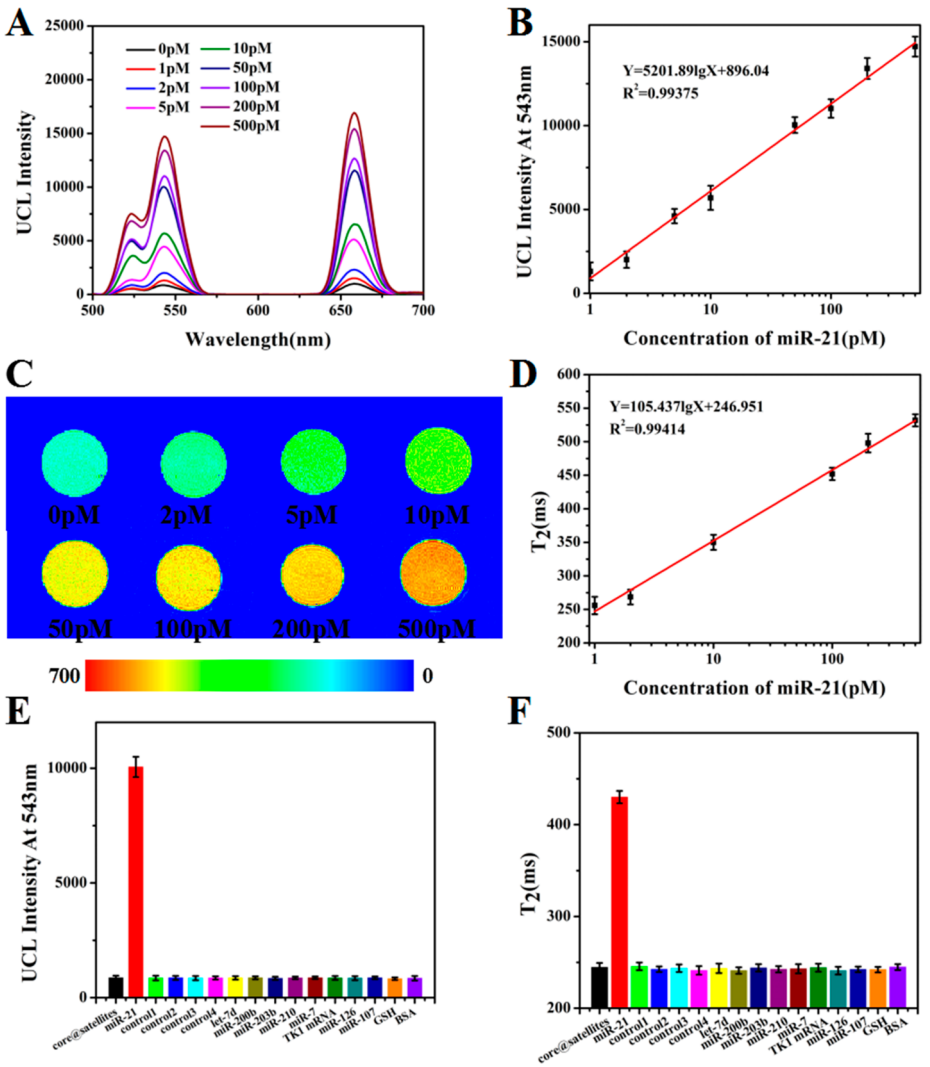

Figure 4. (A) UCL spectra, (B) standard curve of UCL intensity at 543 nm, (C) the T_2-weighted and color-processed images, and (D) standard curve of T_2 value for microRNA-21 detection in vitro. (E) UCL intensity at 543 nm and (F) the T_2 value of core−satellite structures that reacted with the microRNA-21 (50 pM), mutated sequences of microRNA-21 (1 nM, control 1−4), let-7d (1 nM), miR-200b (1 nM), miR-203b (1 nM), miR-210 (1 nM), miR-7 (1 nM), TK1 mRNA (1 nM), miR-126 (1 nM), miR-107 (1 nM), BSA (1 mM), and GSH (1 mM) in vitro.

respectively. In order to facilitate access to the cytoplasm, we modified thiolated PEG (SH-PEG, MW = 5,000) and cell-penetrating peptide (TAT) on the surface of core@satellite nanoprobes. Because of overlap between the emission of UCNPs and the absorption of Fe_xCu_ySe, fluorescence resonance energy transfer (FRET) occurred, resulting in quenching of the UCL intensity of UCNPs in core@satellite nanoprobes. The color of T_2-weighted images varied significantly compared with that of Fe_xCu_ySe, which may be due to the increase in the overall size of the nanoassemblies and/or the influence of Gd doping in UCNPs. When the target miR-21 was present, hybridization of DNA1 and DNA2 was disrupted, leading to separation between UCNPs and Fe_xCu_ySe. The UCL intensity was restored, the T_2 value was increased, and the color of T_2-weighted images changed from turquoise to orange. Consequently, the detection of intracellular miR-21 was based on variation in the UCL intensity and the T_2 value.

Characterization of Fe_xCu_ySe, UCNPs, and Core@Satellite Structures. As shown in Figure S2, the distance between the absorption peak of $Cu_{2-x}Se$ and the dual emission peaks of UCNPs was too large to produce FRET effect. $FeSe_x$ is a type of magnetic NPs, but FRET cannot occur because the absorption of $FeSe_x$ between 500 and 700 nm is too weak to be ignored.[45] Therefore, Fe_xCu_ySe NPs were a better choice for core@satellite structures with dual MRI and UCL signals. The Fe_xCu_ySe NPs was characterized with energy-dispersive X-ray (EDX) spectroscopy mapping, which confirmed the distinct element distribution of Se, Cu, and Fe in the Fe_xCu_ySe (Figure 2B). As shown in the transmission electron microscopy (TEM) images and the dynamic light scattering (DLS) results, Fe_xCu_ySe NPs were 78 ± 3 nm in diameter, whereas UCNPs were 15 ± 2 nm (Figure 2A and Figures S1 and S4). Furthermore, core@satellite structures assembled successfully, as confirmed by TEM, DLS, ultraviolet−visible (UV−vis) absorption spectra, UCL spectra, and MRI. On the basis of statistical analysis of more than 200 TEM images, the yield of core@satellite structures was 85%, and the number of UCNPs on each Fe_xCu_ySe surface was ∼14 (Figure S3B), which indicated the controllable assembly of Fe_xCu_ySe@UCNP core@satellite nanostructures. The amount of DNA1 loaded on a single Fe_xCu_ySe NP were estimated to be 13.7 ± 3.4, and

https://dx.doi.org/10.1021/acsami.0c00434
ACS Appl. Mater. Interfaces XXXX, XXX, XXX−XXX

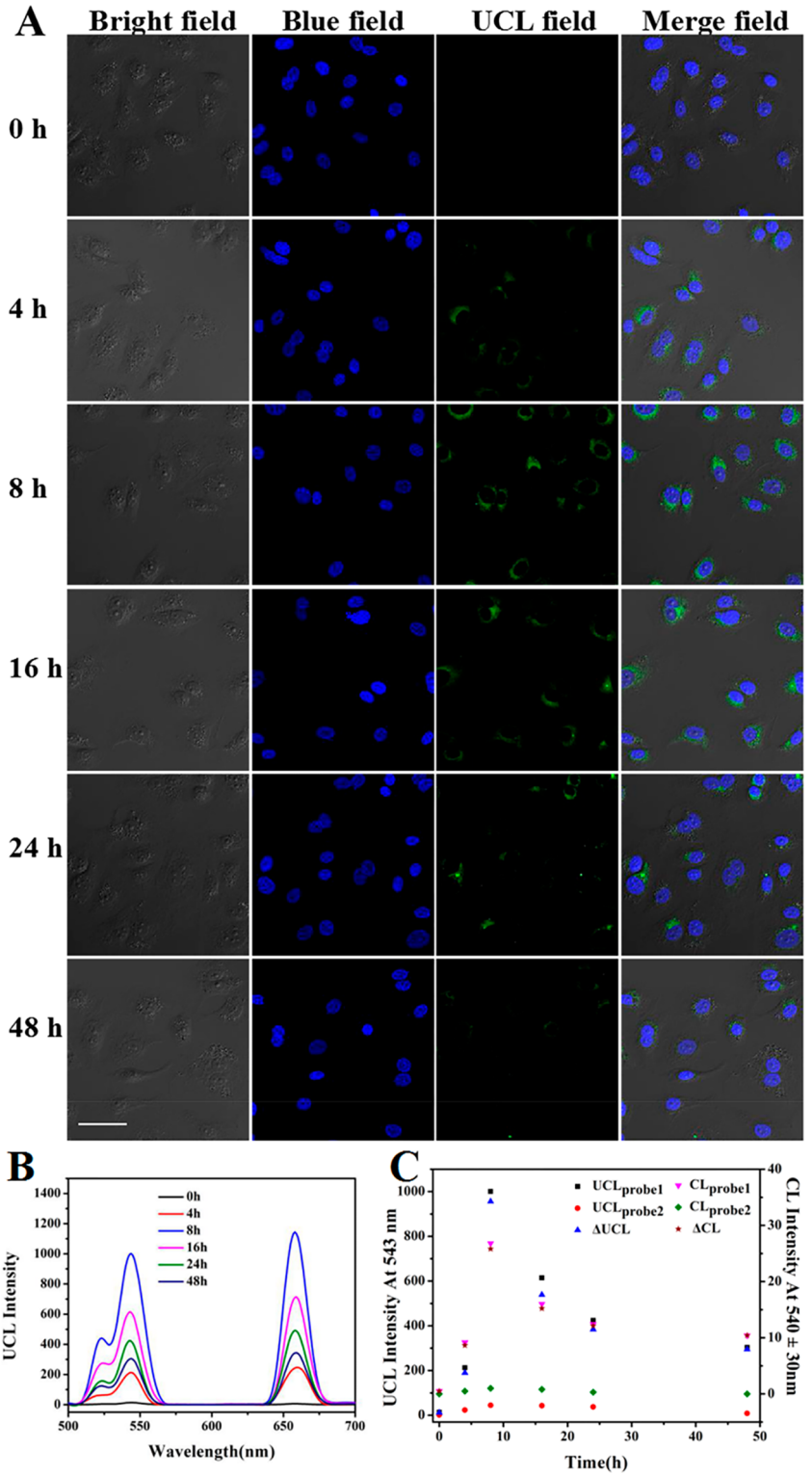

Figure 5. (A) Confocal images and (B) intracellular UCL spectra of probe 1 in MCF-7 cells with the variable incubation time. (C) Statistics analysis of intracellular UCL intensity at 543 nm and CL intensity (540 ± 30 nm) of probe 1 and probe 2 in MCF-7 cells with the variable incubation time (probe 1, assembled with the sequences that could specifically hybridize with miR-21; probe 2, assembled with absolute complementary sequences that had no ability to recognize miR-21). Scale bar: 50 μm.

the number of DNA2 loaded on single UCNP was 1.2 ± 0.8. Compared with Fe_xCu_ySe, the average size of core@satellite structures measured by DLS was significantly increased, and the UV−vis absorption peak displayed a slight red shift (Figure S2 and S4). The UCL intensity of core@satellite structures exhibited significant quenching due to FRET (Figure 2C). The T_2-weighted images of core@satellite structures also changed dramatically in color from orange to turquoise (Figure 2D).

To optimize the dynamic assembly time for core@satellite structures, we used TEM, UCL, UV−vis spectra, and T_2-

https://dx.doi.org/10.1021/acsami.0c00434
ACS Appl. Mater. Interfaces XXXX, XXX, XXX−XXX

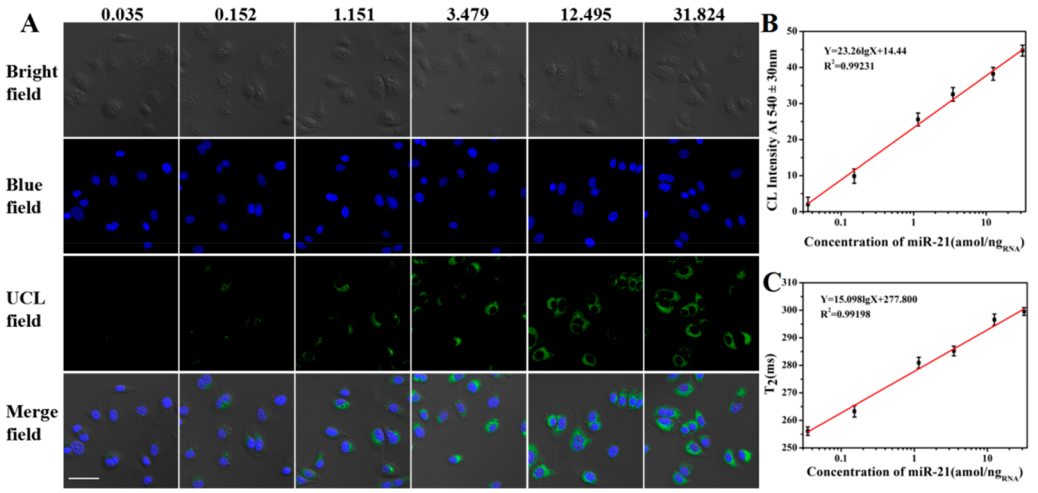

Figure 6. (A) Confocal images of MCF-7 cells with different concentrations of miR-21. Standard curve of (B) CL intensity and (C) the intracellular T_2 value for miR-21 detection. Scale bar: 50 μm.

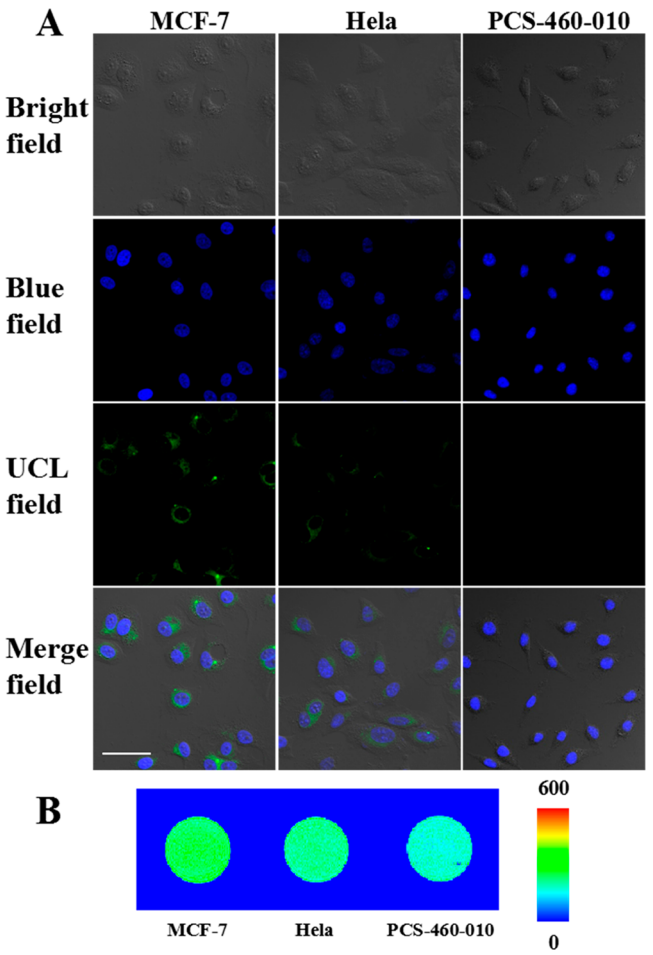

Figure 7. (A) Confocal images and (B) the color-processed T_2-weighted images of core@satellite structures in MCF-7, HeLa, and PCS-460-010 cells.

weighted images for real-time monitoring of the assembly process. As time went on, the amount of UCNPs surrounding Fe_xCu_ySe increased (Figure 3A). At the same time, the UCL intensity gradually reduced, and the color of T_2-weighted images changed (Figure 3B, D). Moreover, the geometry, UCL intensity, and T_2-weighted image color of assemblies no longer changed after 8 h. Thus, 8 h was the optimal assembly time. During dynamic assembly, the shapes of peaks in UV−vis spectra were essentially the same, demonstrating the stability of the assemblies (Figure 3C).

Quantitative Detection of microRNA-21 In Vitro. MiR-21, a useful biomarker overexpressed in a variety of cancers, was selected herein to evaluate the feasibility of this nanoprobe in early diagnosis of diseases. Prior to quantitative detection, the selectivity of core@satellite nanoprobes toward synthetic miRs was investigated using potential interfering substances. Synthetic miR-21 (50 pM), two mutated miR-21 sequences (1 nM, control 1−4), let-7d (1 nM), miR-200b (1 nM), miR-203b (1 nM), miR-210(1 nM), miR-7 (1 nM), TK1 mRNA (1 nM), miR-126 (1 nM), miR-107 (1 nM), bovine serum albumin (BSA, 1 mM), and reduced glutathione (GSH, 1 mM) were added to 1.5 mL centrifuge tubes (each containing 500 μL core@satellite nanoprobes in buffer) and incubated at 37 °C for 2 h (Table S1). In the presence of miR-21, the corresponding UCL intensity and T_2 values were dramatically increased, whereas changes were negligible for other tested miRs, proteins and peptides (Figure 4E, F and Figure S6). Therefore, the core@satellite nanoprobes displayed outstanding specificity for miR-21 detection, whereas proteins and peptides interfered minimally with the detection system. In addition, DNA1-Fe_xCu_ySe and DNA2-UCNPs reacted with the miR-21 for comparison with core@satellite nanoprobes (Figure S7). It showed that core@satellite nanoprobes is the key to detect miR-21.

When detecting synthetic miR-21 in buffer, the UCL intensity and T_2 value increased gradually with increasing concentration of miR-21 (Figure 4A and 4C). Both dual signals displayed a perfect linear correlation with the concentration of miR-21 between 1 and 500 pM (Figure 4B and 4D). In addition, TEM images also confirmed that the higher the concentration of miR-21, the fewer the number of UCNPs (Figure S5). This system was therefore of potential significance in the rapid and accurate detection of intracellular miR-21.

Intracellular MicroRNA-21 Detection. Before applying this probe for the miR-21 detection in living cells, it was necessary to study the stability of the core@satellite nanoprobes in cell culture medium and confirm a lack of cytotoxicity at the optimal dose and incubation time. As shown in Figure

https://dx.doi.org/10.1021/acsami.0c00434
ACS Appl. Mater. Interfaces XXXX, XXX, XXX−XXX

S8, the core@satellite nanoprobes were monodisperse and stable, even after incubating with cell medium for 48 h at 37 °C. MCF-7 cells were cultured with nanoprobes at different concentrations for 8 h to test biocompatibility. The results of Cell Counting Kit-8 analysis found that cell viability was unaffected at concentrations of up to 1.5 mg/mL (Figure S9A). Furthermore, 1.5 mg/mL core@satellite nanoprobes had minimal effect on the viability of living cells after 4−24 h of cultivation (Figure S9B). Thus, 1.5 mg/mL of core@satellite nanoprobes was the optimal dose and had minimal effect on cell viability in subsequent experiments.

Two probes were designed to explore the reactive dynamics of nanoprobes in living cells. Probe1 was assembled using partially complementary sequences that specifically recognize miR-21, and probe2 was assembled using absolute complementary sequences and was unable to capture miR-21. The confocal luminescence (CL) and UCL intensities increased as probe1 captured intracellular miR-21 in MCF-7 cells, and peaked at 8 h (Figure 5). The luminescence intensity then decreased beyond 8 h because of aggregation of nanoprobes in cells. However, the luminescence intensity of cells incubated with probe 2 was substantially unchanged over all time periods (Figure S10 and S11). Meanwhile, the value of ΔUCL ($UCL_{probe1} - UCL_{probe2}$) was highest at 8 h (Figure 5C). Thus, probe 1 could specifically recognize miR-21 because of hybridization of DNA1 and DNA2. And 8 h was therefore chosen as the optimal incubation time for intracellular detection.

Intracellular miR-21 was quantified by transfection of miR-21 or antisense miR-21 into MCF-7 cells followed by qT-PCR (Figure S12). The inherent content of miR-21 in MCF-7 cells was 1.151 amol/ng_{RNA}. After being incubated with core@satellite nanoprobes for 8 h, cells containing different amounts of intracellular miR-21 were quantified in situ by confocal imaging and MRI. With increasing intracellular miR-21 content, dual signals were enhanced and displayed a good linear relationship in the range of 0.035 to 31.824 amol/ng_{RNA} (Figure 6 and Figure S13), with LOD values of 0.0058 and 0.0182 amol/ng_{RNA}, respectively. Compared with other reported detection methods, Fe_xCu_ySe@UCNP core@satellite nanoprobes were more sensitive (Table S2), and capable of detecting miR-21 in living cells at low levels. Moreover, dual UCL and MRI signal detection could be mutually verified and improve the detection accuracy.

To confirm the universality of the developed nanoprobes in different cells, we selected human cervical cancer (HeLa) cells and primary uterine fibroblast (PCS-460-010) cells as representative cell lines. As shown in Figure 7, the CL intensity and T_2 value of MCF-7 cells were higher than those of HeLa cells and PCS-460-010 cells, and both signal intensities were weakest for PCS-460-010 cells. The content of miR-21 in HeLa cells was 0.366 ± 0.025 and 0.387 ± 0.010 amol/ng_{RNA}, determined respectively by confocal imaging and MRI, whereas levels in PCS-460-010 cells were too low to determine. These results demonstrated that the nanoprobes possessed good universality and feasibility for use in various cell lines.

CONCLUSIONS

In conclusion, core@satellite nanoprobes were assembled from Fe_xCu_ySe and UCNPs and used for intracellular miR-21 detection based on dual UCL and MRI signals. The LOD values for miR-21 were 0.0058 and 0.0182 mol/ng_{RNA} in living cells, respectively. This ultrasensitive detection strategy was suitable not only for in situ miRs imaging and quantification but also for general biomarker detection because the sequence of DNA in core@satellite nanoprobes could be altered. In addition, nanoprobes could be applied for early medical diagnosis and bioimaging in life science research.

ASSOCIATED CONTENT

Supporting Information

The Supporting Information is available free of charge at https://pubs.acs.org/doi/10.1021/acsami.0c00434.

Experimental section and methods, more TEM images, UV−vis absorption spectra, DLS size distribution, and UCL spectra of Fe_xCu_ySe; cell viability assays; confocal images and intracellular UCL spectra of probe 2; DNA and RNA sequences; and comparison of complementary detection methods (PDF)

AUTHOR INFORMATION

Corresponding Authors

Xiaoling Wu − *International Joint Research Laboratory for Biointerface and Biodetection, State Key Lab of Food Science and Technology and School of Food Science and Technology, Jiangnan University, Wuxi, Jiangsu 214122, P.R. China*; Email: wxl@jiangnan.edu.cn

Hua Kuang − *International Joint Research Laboratory for Biointerface and Biodetection, State Key Lab of Food Science and Technology and School of Food Science and Technology, Jiangnan University, Wuxi, Jiangsu 214122, P.R. China*; Email: kuangh@jiangnan.edu.cn

Authors

Xiaoqian Jiang − *International Joint Research Laboratory for Biointerface and Biodetection, State Key Lab of Food Science and Technology and School of Food Science and Technology, Jiangnan University, Wuxi, Jiangsu 214122, P.R. China*

Changlong Hao − *International Joint Research Laboratory for Biointerface and Biodetection, State Key Lab of Food Science and Technology and School of Food Science and Technology, Jiangnan University, Wuxi, Jiangsu 214122, P.R. China*

Hongyu Zhang − *International Joint Research Laboratory for Biointerface and Biodetection, State Key Lab of Food Science and Technology and School of Food Science and Technology, Jiangnan University, Wuxi, Jiangsu 214122, P.R. China*

Liguang Xu − *International Joint Research Laboratory for Biointerface and Biodetection, State Key Lab of Food Science and Technology and School of Food Science and Technology, Jiangnan University, Wuxi, Jiangsu 214122, P.R. China*

Maozhong Sun − *International Joint Research Laboratory for Biointerface and Biodetection, State Key Lab of Food Science and Technology and School of Food Science and Technology, Jiangnan University, Wuxi, Jiangsu 214122, P.R. China*

Chuanlai Xu − *International Joint Research Laboratory for Biointerface and Biodetection, State Key Lab of Food Science and Technology and School of Food Science and Technology, Jiangnan University, Wuxi, Jiangsu 214122, P.R. China*; orcid.org/0000-0002-5639-7102

Complete contact information is available at: https://pubs.acs.org/10.1021/acsami.0c00434

Notes

The authors declare no competing financial interest.

https://dx.doi.org/10.1021/acsami.0c00434
ACS Appl. Mater. Interfaces XXXX, XXX, XXX−XXX

■ ACKNOWLEDGMENTS

This work was financially supported by the National Natural Science Foundation of China and the Natural Science Foundation of Jiangsu Province (21977038, 51902136, 21874058, 51802125, BK20180029).

■ REFERENCES

(1) Cen, Y.; Deng, W. J.; Yang, Y.; Yu, R. Q.; Chu, X. Core-Shell-Shell Multifunctional Nanoplatform for Intracellular Tumor-Related mRNAs Imaging and Near-Infrared Light Triggered Photodynamic-Photothermal Synergistic Therapy. *Anal. Chem.* **2017**, *89* (19), 10321−10328.

(2) Ma, W.; Sun, M.; Fu, P.; Li, S.; Xu, L.; Kuang, H.; Xu, C. A Chiral-Nanoassemblies-Enabled Strategy for Simultaneously Profiling Surface Glycoprotein and MicroRNA in Living Cells. *Adv. Mater.* **2017**, *29* (42), 1703410.

(3) Qu, A.; Xu, L.; Sun, M.; Liu, L.; Kuang, H.; Xu, C. Photoactive Hybrid AuNR-Pt@Ag2S Core-Satellite Nanostructures for Near-Infrared Quantitive Cell Imaging. *Adv. Funct. Mater.* **2017**, *27* (46), 1703408.

(4) Laurenti, M.; Paez-Perez, M.; Algarra, M.; Alonso-Cristobal, P.; Lopez-Cabarcos, E.; Mendez-Gonzalez, D.; Rubio-Retama, J. Enhancement of the Upconversion Emission by Visible-to-Near-Infrared Fluorescent Graphene Quantum Dots for miRNA Detection. *ACS Appl. Mater. Interfaces* **2016**, *8* (20), 12644−12651.

(5) Gao, R.; Hao, C.; Xu, L.; Xu, C.; Kuang, H. Spiny Nanorod and Upconversion Nanoparticle Satellite Assemblies for Ultrasensitive Detection of Messenger RNA in Living Cells. *Anal. Chem.* **2018**, *90* (8), 5414−5421.

(6) Ren, H.; Long, Z.; Shen, X.; Zhang, Y.; Sun, J.; Ouyang, J.; Na, N. Sandwich DNA Hybridization Fluorescence Resonance Energy-Transfer Strategy for miR-122 Detection by Core-Shell Upconversion Nanoparticles. *ACS Appl. Mater. Interfaces* **2018**, *10* (30), 25621−25628.

(7) Hao, T.; Wu, X.; Xu, L.; Liu, L.; Ma, W.; Kuang, H.; Xu, C. Ultrasensitive Detection of Prostate-Specific Antigen and Thrombin Based on Gold-Upconversion Nanoparticle Assembled Pyramids. *Small* **2017**, *13* (19), 1603944.

(8) Liu, C.; Chen, C.; Li, S.; Dong, H.; Dai, W.; Xu, T.; Liu, Y.; Yang, F.; Zhang, X. Target-Triggered Catalytic Hairpin Assembly-Induced Core-Satellite Nanostructures for High-Sensitive "Off-to-On" SERS Detection of Intracellular MicroRNA. *Anal. Chem.* **2018**, *90* (17), 10591−10599.

(9) Zhao, X.; Xu, L.; Sun, M.; Ma, W.; Wu, X.; Kuang, H.; Wang, L.; Xu, C. Gold-Quantum Dot Core-Satellite Assemblies for Lighting Up MicroRNA In Vitro and In Vivo. *Small* **2016**, *12* (34), 4662−4668.

(10) Yang, L.; Zhang, K.; Bi, S.; Zhu, J.-J. Dual-Acceptor-Based Upconversion Luminescence Nanosensor with Enhanced Quenching Efficiency for in Situ Imaging and Quantification of MicroRNA in Living Cells. *ACS Appl. Mater. Interfaces* **2019**, *11* (42), 38459−38466.

(11) Mendez-Gonzalez, D.; Lahtinen, S.; Laurenti, M.; Lopez-Cabarcos, E.; Rubio-Retama, J.; Soukka, T. Photochemical Ligation to Ultrasensitive DNA Detection with Upconverting Nanoparticles. *Anal. Chem.* **2018**, *90* (22), 13385−13392.

(12) Zhang, K.; Song, S.; Huang, S.; Yang, L.; Min, Q.; Wu, X.; Lu, F.; Zhu, J.-J. Lighting Up MicroRNA in Living Cells by the Disassembly of Lock-Like DNA-Programmed UCNPs-AuNPs through the Target Cycling Amplification Strategy. *Small* **2018**, *14* (40), 1802292.

(13) Ding, Q.; Zhan, Q.; Zhou, X.; Zhang, T.; Xing, D. Theranostic Upconversion Nanobeacons for Tumor mRNA Ratiometric Fluorescence Detection and Imaging-Monitored Drug Delivery. *Small* **2016**, *12* (43), 5944−5953.

(14) Liang, T.; Li, Z.; Song, D.; Shen, L.; Zhuang, Q.; Liu, Z. Modulating the Luminescence of Upconversion Nanoparticles with Heavy Metal Ions: A New Strategy for Probe Design. *Anal. Chem.* **2016**, *88* (20), 9989−9995.

(15) Peng, J.; Xu, W.; Teoh, C. L.; Han, S.; Kim, B.; Samanta, A.; Er, J. C.; Wang, L.; Yuan, L.; Liu, X.; Chang, Y.-T. High-Efficiency in Vitro and in Vivo Detection of Zn^{2+} by Dye-Assembled Upconversion Nanoparticles. *J. Am. Chem. Soc.* **2015**, *137* (6), 2336−2342.

(16) Li, L.-L.; Lu, Y. Regiospecific Hetero-Assembly of DNA-Functionalized Plasmonic Upconversion Superstructures. *J. Am. Chem. Soc.* **2015**, *137* (16), 5272−5275.

(17) Li, S.; Xu, L.; Sun, M.; Wu, X.; Liu, L.; Kuang, H.; Xu, C. Hybrid Nanoparticle Pyramids for Intracellular Dual MicroRNAs Biosensing and Bioimaging. *Adv. Mater.* **2017**, *29* (19), 1606086.

(18) Sun, M.; Qu, A.; Hao, C.; Wu, X.; Xu, L.; Xu, C.; Kuang, H. Chiral Upconversion Heterodimers for Quantitative Analysis and Bioimaging of Antibiotic-Resistant Bacteria In Vivo. *Adv. Mater.* **2018**, *30* (50), 1804241.

(19) Sun, M.; Xu, L.; Ma, W.; Wu, X.; Kuang, H.; Wang, L.; Xu, C. Hierarchical Plasmonic Nanorods and Upconversion Core-Satellite Nanoassemblies for Multimodal Imaging-Guided Combination Phototherapy. *Adv. Mater.* **2016**, *28* (5), 898−904.

(20) Ma, W.; Fu, P.; Sun, M.; Xu, L.; Kuang, H.; Xu, C. Dual Quantification of MicroRNAs and Telomerase in Living Cells. *J. Am. Chem. Soc.* **2017**, *139* (34), 11752−11759.

(21) Qu, A.; Wu, X.; Xu, L.; Liu, L.; Ma, W.; Kuang, H.; Xu, C. SERS- and luminescence-active Au-Au-UCNP trimers for attomolar detection of two cancer biomarkers. *Nanoscale* **2017**, *9* (11), 3865−3872.

(22) Wang, F.; Han, Y.; Wang, S.; Ye, Z.; Wei, L.; Xiao, L. Single-Particle LRET Aptasensor for the Sensitive Detection of Aflatoxin B-1 with Upconversion Nanoparticles. *Anal. Chem.* **2019**, *91* (18), 11856−11863.

(23) Bogdanov, A. A.; Dixon, A. J.; Gupta, S.; Zhang, L.; Zheng, S.; Shazeeb, M. S.; Zhang, S.; Klibanov, A. L. Synthesis and Testing of Modular Dual-Modality Nanoparticles for Magnetic Resonance and Multispectral Photoacoustic Imaging. *Bioconjugate Chem.* **2016**, *27* (2), 383−390.

(24) Louie, A. Y. Multimodality Imaging Probes: Design and Challenges. *Chem. Rev.* **2010**, *110* (5), 3146−3195.

(25) Zhao, Z.; Fan, H.; Zhou, G.; Bai, H.; Liang, H.; Wang, R.; Zhang, X.; Tan, W. Activatable Fluorescence/MRI Bimodal Platform for Tumor Cell Imaging via MnO2 Nanosheet-Aptamer Nanoprobe. *J. Am. Chem. Soc.* **2014**, *136* (32), 11220−11223.

(26) Fallows, T. W.; McGrath, A. J.; Silva, J.; McAdams, S. G.; Marchesi, A.; Tuna, F.; Flitsch, S. L.; Tilley, R. D.; Webb, S. J. High-throughput chemical and chemoenzymatic approaches to saccharide-coated magnetic nanoparticles for MRI. *Nanoscale Adv.* **2019**, *1* (9), 3597−3606.

(27) Li, Y.; Hu, X.; Ding, D.; Zou, Y.; Xu, Y.; Wang, X.; Zhang, Y.; Chen, L.; Chen, Z.; Tan, W. In situ targeted MRI detection of Helicobacter pylori with stable magnetic graphitic nanocapsules. *Nat. Commun.* **2017**, *8*, 15653.

(28) Wang, J.; Zhang, H.; Ni, D.; Fan, W.; Qu, J.; Liu, Y.; Jin, Y.; Cui, Z.; Xu, T.; Wu, Y.; Bu, W.; Yao, Z. High-Performance Upconversion Nanoprobes for Multimodal MR Imaging of Acute Ischemic Stroke. *Small* **2016**, *12* (26), 3591−3600.

(29) Wu, Y.; Li, D.; Zhou, F.; Liang, H.; Liu, Y.; Hou, W.; Yuan, Q.; Zhang, X.; Tan, W. Versatile in situ synthesis of MnO2 nanolayers on upconversion nanoparticles and their application inactivatable fluorescence and MRI imaging. *Chem. Sci.* **2018**, *9* (24), 5427−5434.

(30) Duan, M.; Xia, F.; Li, T.; Shapter, J. G.; Yang, S.; Li, Y.; Gao, G.; Cui, D. Matrix metalloproteinase-2-targeted superparamagnetic Fe3O4-PEG-G5-MMP2@Ce6 nanoprobes for dual-mode imaging and photodynamic therapy. *Nanoscale* **2019**, *11* (39), 18426−18435.

(31) Li, C.; Chen, T.; Ocsoy, I.; Zhu, G.; Yasun, E.; You, M.; Wu, C.; Zheng, J.; Song, E.; Huang, C. Z.; Tan, W. Gold- Coated Fe 3 O 4 Nanoroses with Five Unique Functions for Cancer Cell Targeting, Imaging, and Therapy. *Adv. Funct. Mater.* **2014**, *24* (12), 1772−1780.

(32) Liu, B.; Hu, F.; Zhang, J.; Wang, C.; Li, L. A Biomimetic Coordination Nanoplatform for Controlled Encapsulation and Delivery of Drug-Gene Combinations. *Angew. Chem., Int. Ed.* **2019**, *58* (26), 8804−8808.

https://dx.doi.org/10.1021/acsami.0c00434
ACS Appl. Mater. Interfaces XXXX, XXX, XXX−XXX

(33) Zhang, F.; Li, F.; Lu, G.-H.; Nie, W.; Zhang, L.; Lv, Y.; Bao, W.; Gao, X.; Wei, W.; Pu, K.; Xie, H.-Y. Engineering Magnetosomes for Ferroptosis/Immunomodulation Synergism in Cancer. *ACS Nano* **2019**, *13* (5), 5662−5673.
(34) Han, Y.; An, Y.; Jia, G.; Wang, X.; He, C.; Ding, Y.; Tang, Q. Theranostic micelles based on upconversion nanoparticles for dual-modality imaging and photodynamic therapy in hepatocellular carcinoma. *Nanoscale* **2018**, *10* (14), 6511−6523.
(35) Li, C.; Yang, D.; Ma, P. a.; Chen, Y.; Wu, Y.; Hou, Z.; Dai, Y.; Zhao, J.; Sui, C.; Lin, J. Multifunctional Upconversion Mesoporous Silica Nanostructures for Dual Modal Imaging and In Vivo Drug Delivery. *Small* **2013**, *9* (24), 4150−4159.
(36) Wang, L.; Gao, C.; Liu, K.; Liu, Y.; Ma, L.; Liu, L.; Du, X.; Zhou, J. Cypate-Conjugated Porous Upconversion Nanocomposites for Programmed Delivery of Heat Shock Protein 70 Small Interfering RNA for Gene Silencing and Photothermal Ablation. *Adv. Funct. Mater.* **2016**, *26* (20), 3480−3489.
(37) Zhao, Z.; Xu, K.; Fu, C.; Liu, H.; Lei, M.; Bao, J.; Fu, A.; Yu, Y.; Zhang, W. Interfacial engineered gadolinium oxide nanoparticles for magnetic resonance imaging guided microenvironment-mediated synergetic chemodynamic/photothermal therapy. *Biomaterials* **2019**, *219*, 119379.
(38) Li, Y.; Chen, T.; Tan, W.; Talham, D. R. Size-Dependent MRI Relaxivity and Dual Imaging with Eu0.2Gd0.8PO4 center dot H2O Nanoparticles. *Langmuir* **2014**, *30* (20), 5873−5879.
(39) Li, Y.; Tang, J.; He, L.; Liu, Y.; Liu, Y.; Chen, C.; Tang, Z. Core-Shell Upconversion Nanoparticle@Metal-Organic Framework Nanoprobes for Luminescent/Magnetic Dual-Mode Targeted Imaging. *Adv. Mater.* **2015**, *27* (27), 4075−4080.
(40) Ma, W.; Hao, C.; Ma, W.; Xing, C.; Yan, W.; Kuang, H.; Wang, L.; Xu, C. Wash-free magnetic oligonucleotide probes-based NMR sensor for detecting the Hg ion. *Chem. Commun.* **2011**, *47* (46), 12503−12505.
(41) Zhong, D.; Zhao, J.; Li, Y.; Qiao, Y.; Wei, Q.; He, J.; Xie, T.; Li, W.; Zhou, M. Laser-triggered aggregated cubic alpha-Fe2O3@Au nanocomposites for magnetic resonance imaging and photothermal/enhanced radiation synergistic therapy. *Biomaterials* **2019**, *219*, 119369.
(42) Zhang, S.; Huang, Q.; Zhang, L.; Zhang, H.; Han, Y.; Sun, Q.; Cheng, Z.; Qin, H.; Dou, S.; Li, Z. Vacancy engineering of Cu2-xSe nanoparticles with tunable LSPR and magnetism for dual-modal imaging guided photothermal therapy of cancer. *Nanoscale* **2018**, *10* (7), 3130−3143.
(43) Yi, Z.; Luo, Z.; Barth, N. D.; Meng, X.; Liu, H.; Bu, W.; All, A.; Vendrell, M.; Liu, X. In Vivo Tumor Visualization through MRI Off-On Switching of NaGdF4-CaCO3 Nanoconjugates. *Adv. Mater.* **2019**, *31* (37), 1901851.
(44) Xia, A.; Gao, Y.; Zhou, J.; Li, C.; Yang, T.; Wu, D.; Wu, L.; Li, F. Core-shell NaYF4:Yb3+,Tm3+@FexOy nanocrystals for dual-modality T-2-enhanced magnetic resonance and NIR-to-NIR upconversion luminescent imaging of small-animal lymphatic node. *Biomaterials* **2011**, *32* (29), 7200−7208.
(45) Mao, X.; Kim, J.-G.; Han, J.; Jung, H. S.; Lee, S. G.; Kotov, N. A.; Lee, J. Phase-Pure FeSex (x = 1, 2) Nanoparticles with One- and Two-Photon Luminescence. *J. Am. Chem. Soc.* **2014**, *136* (20), 7189−7192.

https://dx.doi.org/10.1021/acsami.0c00434
ACS Appl. Mater. Interfaces XXXX, XXX, XXX−XXX